

Vasant K. Dasika, John A. White and H. Steven Colburn

J Neurophysiol 97:3449-3459, 2007. First published Aug 16, 2006; doi:10.1152/jn.00669.2005

You might find this additional information useful...

This article cites 35 articles, 14 of which you can access free at:

<http://jn.physiology.org/cgi/content/full/97/5/3449#BIBL>

Updated information and services including high-resolution figures, can be found at:

<http://jn.physiology.org/cgi/content/full/97/5/3449>

Additional material and information about *Journal of Neurophysiology* can be found at:

<http://www.the-aps.org/publications/jn>

This information is current as of July 18, 2007 .

Simple Models Show the General Advantages of Dendrites in Coincidence Detection

Vasant K. Dasika,^{1,2} John A. White,^{1,3} and H. Steven Colburn^{1,2}

¹Department of Biomedical Engineering, ²Hearing Research Center, and ³Center for BioDynamics, Boston University, Boston, Massachusetts

Submitted 27 June 2005; accepted in final form 26 July 2006

Dasika VK, White JA, Colburn HS. Simple models show the general advantages of dendrites in coincidence detection. *J Neurophysiol* 97: 3449–3459, 2007. First published August 16, 2006; doi:10.1152/jn.00669.2005. Dendrites can influence and improve information processing in single neurons. Here, simple models are used to elucidate mechanisms underlying the dendritic enhancement of coincidence detection. We focus on coincidence-detecting cells in the auditory system, which have bipolar dendrites and show acute sensitivity to interaural time difference (ITD), a critical cue for spatial hearing. A three-compartment model consisting of a single-compartment soma and two single-compartment dendrites is primarily used, although multiple-compartment dendrites are also tested. Two varieties of somata, with and without active ion channels, are studied. Using constant conductance inputs, we show analytically that the somatic response to balanced bilateral inputs is largest, whereas the response monotonically decreases as the input distribution becomes increasingly monolateral. This enhancement is a consequence of the sublinear saturating dendritic voltage response to conductance input and occurs when dendrites are composed of a single compartment or either a finite number or an infinite number (i.e., a cable) of compartments. Longer, thinner dendrites or greater numbers of compartments increase the enhancement of the somatic response to bilateral input. The time-independent dendritic enhancement, moreover, underlies improved coincidence detection of time-varying input. Coincidence sensitivity to a pair of conductance pulses and rate-ITD modulation to low-frequency (400-Hz) periodic inputs increases with dendritic length. These findings are related to the length gradient in the avian system, where low characteristic frequency (CF) cells have long dendrites and high CF cells have short dendrites. We conclude that dendrites fundamentally improve coincidence detection, increasing the computational power of many neurons in the nervous system.

INTRODUCTION

Neurons across the nervous system exhibit great diversity in their dendritic morphology and information processing characteristics. Dendrites likely influence neural plasticity (e.g., Williams and Stuart 2002; Xu et al. 2006) and sensory processing (e.g., Agmon-Snir et al. 1998; Archie and Mel 2001). In the auditory system, the initial site of binaural interaction is a key site to study dendritic processing. Single cells in mammalian medial superior olive (MSO) and avian nucleus laminaris (NL) have stereotypical bipolar dendrites. Ascending neural inputs from each ear excite a distinct dendrite (Boord 1968; Parks and Rubel 1975; Ramón y Cajal 1908; Smith and Rubel 1979; Stotler 1953). By performing coincidence detection on the phase-locked inputs from the two sides (Jeffress 1948; for review see Joris et al. 1998), these cells show acute sensitivity to the submillisecond difference in the time of

arrival of sound to the two ears. This interaural time difference (ITD) is a critical cue for spatial hearing (e.g., Brown 1994; Durlach and Colburn 1978).

Computational models (Agmon-Snir et al. 1998; Grau-Serrat et al. 2003; Simon et al. 1999) show that dendrites can enhance coincidence detection in single NL and MSO cells. Agmon-Snir et al. (1998) first demonstrated that cell models with dendrites show greater sensitivity to ITD compared with single-compartment (i.e., point-neuron) models. Coincidence sensitivity, moreover, increased as dendrites became thinner (Agmon-Snir et al. 1998). Using a biophysically detailed model, Grau-Serrat et al. (2003) additionally found an “optimal” dendritic length for a given stimulus frequency, such that maximal coincidence sensitivity was achieved with longer dendrites for lower-frequency inputs, whereas optimal dendritic length decreased as stimulation frequency increased. The findings of Grau-Serrat and colleagues (2003) are consistent with the anatomical dendritic length gradient in chicken, owl, and emu, in which lower characteristic frequency (CF) cells have longer dendrites (Carr and Boudreau 1993; MacLeod et al. 2006; Smith 1981; Smith and Rubel 1979).

Herein, we identify fundamental mechanisms that underlie the dendritic improvement of coincidence detection. For the first time, analytical and computational techniques are used in combination to elucidate dendritic integration and coincidence detection. We use simple, few-parameter cable and compartmental models to describe phenomena observed empirically and in more complete models. This work is similar to that of Pinsky and Rinzel (1994), in which a reduced two-compartment model was used to account for many properties observed in a more complete, 19-compartment model of a CA3 pyramidal cell constructed by Traub and colleagues (1991). Our results extend the critical finding put forth by Rall that inputs distributed to distinct dendritic branches elicit stronger downstream excitatory postsynaptic potentials (EPSPs) compared with stimulation of a common dendritic branch (Rall 1964, 1970). Overall, we find that dendrites fundamentally enhance the spatial integration of inputs, improving coincidence detection in single neurons.

METHODS

We use both analytical and computational techniques to determine the responses of model cells to various sets of inputs. Inputs are either static (i.e., constant) or dynamic. The following three sections describe the model cells, their inputs, and the analytical and computational methods used.

Address for reprint requests and other correspondence: V. K. Dasika, VMBHRC, University of Washington, Box 357923, Seattle, WA 98195 (E-mail: vasant.dasika@gmail.com).

The costs of publication of this article were defrayed in part by the payment of page charges. The article must therefore be hereby marked “advertisement” in accordance with 18 U.S.C. Section 1734 solely to indicate this fact.

Cell models

Each model cell consists of a single-compartment soma with two identical passive dendritic sections attached to the soma. Single-compartment dendritic sections are the primary example, although dendrites made up of multiple compartments are also tested. A drawing of an MSO cell (Smith 1995) and an abstracted model cell are shown in Fig. 1, *A* and *B*, respectively. Synaptic inputs are conductance changes that excite the two dendrites at symmetrical spatial locations. Conductance parameters G_1 and G_2 represent the inputs from the left and right sides, respectively. The voltage source V_d is depolarizing with respect to the somatic rest potential V_{rest} . Thus inputs are purely excitatory.

COMPARTMENT MODEL DENDRITES. The cell model in Fig. 1*B* has two single-compartment dendritic sections. The model thus has three

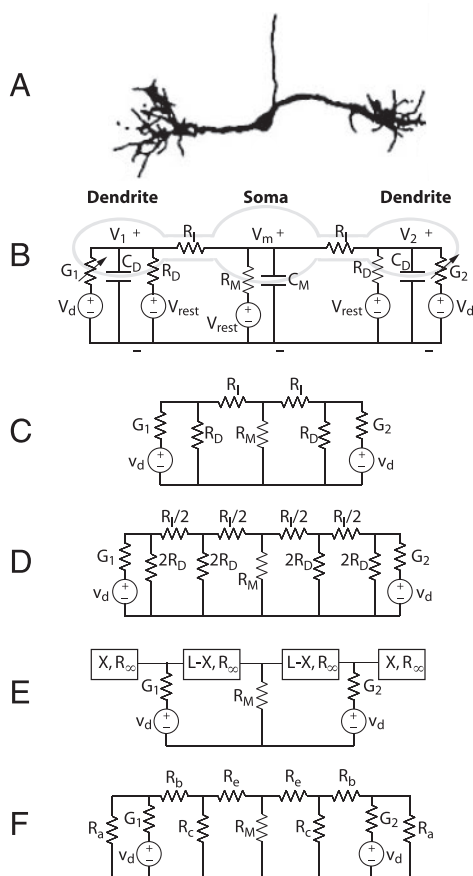


FIG. 1. *A*: drawing of a medial superior olive (MSO) cell (Smith 1995, used with permission). *B*–*F*: bipolar dendritic models with synaptic input. Models do not specify an axon. G_1 and G_2 are the input conductances to each dendrite. V_m is the somatic potential; V_1 and V_2 are the dendritic potentials. *B*: model with single compartment dendrites (circuit is 3 total compartments). Parameters are: soma resistance R_M , soma capacitance C_M , intercompartmental resistance R_I , resting membrane voltage V_{rest} , synaptic driving voltage V_d , dendritic resistance R_D , and dendritic capacitance C_D . *C*–*E*: multicompartment models with constant inputs. Capacitors are not shown because the response is time independent. V_{rest} in *B* has been normalized by replacing V_d with v_d , where $v_d = V_d - V_{rest}$. *C*: constant-inputs reduction of *B*. *D*: each dendritic section is 2 compartments (circuit is 5 total compartments). “Dendrite size” equals that in *B* or *C*. *E*: cable dendrite model with parameters: normalized distance X , electrotonic length L , and electrical properties specified by R_∞ (see METHODS). Inputs can be placed between the dendrite ends ($X = 0$) and the soma ($X = L$). *F*: any multicompartment or cable model can be represented by this 5-compartment model.

(total) compartments. The amount of compartment separation is determined by the resistor R_I , the dendritic load resistance by R_D , and the dendritic capacitance by C_D .

Most of the simulations test cases when the three-compartment model (Fig. 1*B*) approximates a dendritic cable. A cylinder with a fixed diameter ($4 \mu\text{m}$) and a length that is either constant ($150 \mu\text{m}$) or that varies ($0, 50, \text{ or } 150 \mu\text{m}$) is assumed. These diameter (d) and length (l) ranges are consistent with those observed anatomically (Smith 1981; Smith and Rubel 1979) and used in previous models (Agmon-Snir et al. 1998; Grau-Serrat et al. 2003). Standard values for the specific axial resistance R_i ($200 \Omega\cdot\text{cm}$), specific membrane resistance R_d ($1,700 \Omega\cdot\text{cm}^2$), and specific membrane capacitance C_d ($1 \mu\text{F}/\text{cm}^2$) are used, as in previous models. The following three equations relate the three-compartment model dendritic variables with the cable parameters: $R_I = R_i l / [\pi(d/2)^2]$, $R_D = R_d / (\pi d l)$, $C_D = C_d \pi d l$. As the dendritic length l increases, the compartmental parameters R_I , R_D , and C_D all vary in such a manner that R_I and C_D increase, whereas R_D decreases. Some analyses also test the effects of increasing the number of dendritic compartments assuming the same cable; e.g., two-compartment dendrites are shown in Fig. 1*D*, in comparison to the single-compartment dendrites in Fig. 1*C*. Capacitances are not shown in Fig. 1, *C* and *D* because circuit currents and voltages do not change with time in response to constant inputs.

Some simulations (Fig. 5) test the effects of varying just the intercompartmental resistance R_I in the three-compartment model, where R_D and C_D are fixed. In these cases, $R_D C_D$ is 1 ms and R_D is $80 \text{ M}\Omega$. Here, the surface area of the single “dendritic compartment” is assumed to be half that of the soma (R_M is $40 \text{ M}\Omega$ for passive somata), resulting in a dendritic resistance R_D that is twice the somatic resistance (R_M). Although there is no clear connection to a dendritic cable, these cases isolate the effects of a key parameter, the dendrite-to-soma coupling resistance R_I , on dendritic integration (see RESULTS).

The differential equations describing the model shown in Fig. 1*B* are given by

$$C_D \frac{dV_1}{dt} + \frac{V_1 - V_{rest}}{R_D} + G_1(V_1 - V_d) + \frac{V_1 - V_m}{R_I} = 0 \quad (1)$$

$$C_M \frac{dV_m}{dt} + \frac{V_m - V_{rest}}{R_M} + \frac{V_m - V_1}{R_I} + \frac{V_m - V_2}{R_I} = 0 \quad (2)$$

$$C_D \frac{dV_2}{dt} + \frac{V_2 - V_{rest}}{R_D} + G_2(V_2 - V_d) + \frac{V_2 - V_m}{R_I} = 0 \quad (3)$$

where V_1 , V_m , and V_2 represent the voltages in the left dendritic, somatic, and right dendritic compartments, respectively. We generally calculate the somatic voltage response for arbitrary input patterns G_1 and G_2 . If G_1 and G_2 are constant, the capacitance currents are null and models can be represented by the resistive networks shown in Fig. 1, *C* and *D*.

CABLE DENDRITES. Dendritic sections made up of cables having an infinite number of compartments are also tested. A model with finite-length cable dendrites is shown in Fig. 1*E*. To analytically solve this circuit, standard forms for the voltage V along a finite-length section of cable that is terminated with a load resistance R_{out} and for the input resistance (R_{in}) of this cable section are used (cf. Koch 1999). These expressions are given in terms of electrotonic length L in the following equations

$$V(Z) = V(0) \frac{\cosh(L - Z) + \frac{R_z}{R_{out}} \sinh(L - Z)}{\cosh(L) + \frac{R_z}{R_{out}} \sinh(L)} \quad (4)$$

$$R_{in} = R_{\infty} \frac{1 + \frac{R_{\infty}}{R_{out}} \tanh(L)}{\frac{R_{\infty}}{R_{out}} + \tanh(L)} \quad (5)$$

where

$$R_{\infty} = \frac{2\sqrt{R_l R_d}}{\pi d^{3/2}} \quad (6)$$

In Eqs. 4 to 6, $V(0)$ is voltage at the proximal end of the cable, Z represents the “electrotonic distance” along the cable from the proximal end (i.e., $Z = z/\lambda$, where z is distance from the proximal end and λ is the space constant of the cable equaling $[dR_d/(4R_l)]^{1/2}$), L is the electrotonic length of the cable (i.e., $L = l/\lambda$), and R_{∞} represents the input resistance of an infinite-length cable with the same diameter and electrical properties. Dendritic cable theory is reviewed by Koch (1999).

SOMATA. Two categories of somata are investigated: passive somata, consisting of a fixed-impedance soma as shown in Fig. 1B, and active somata, consisting of a published auditory-neuron model with voltage-gated ion channels (Rothman et al. 1993). For passive somata, V_d is replaced by v_d , the value of the synaptic driving battery relative to the somatic rest potential (i.e., $v_d = V_d - V_{rest}$). This modification effectively removes V_{rest} from the circuit with no loss of generality (example circuits are shown in Fig. 1, C–F).

For active somata, the model resembles that shown in Fig. 1B, except that the passive soma model is replaced in its entirety by the single-compartment, active model specified by Rothman et al. (1993). For these active somata cases, the term in Eq. 2 that describes the current through the somatic membrane resistance, $(V_m - V_{rest})/R_M$, is replaced by the sum of the four currents (sodium, delayed-rectifier potassium, leakage, and low-threshold potassium currents) specified by Rothman and colleagues (1993). Furthermore, for active somata cases, V_{rest} in Eqs. 1 and 3 represents the resting membrane potential of the Rothman et al. (1993) model (–60 mV at 38°C). The somatic voltage is the primary response variable for both passive and active model cases. The response is defined as the maximal somatic depolarization in the passive soma case and by the presence of an action potential in the active soma case.

Input model

Inputs are characterized by either static (i.e., constant) or dynamic conductances. In the auditory system, these conductance changes model the bilateral excitatory input from mammalian cochlear nucleus or avian nucleus magnocellularis cells. For dynamic inputs, transient conductance changes are triggered at specified times. Trigger times are either deterministic for isolated pairs of pulses or stochastic for periodic pulse trains. For dynamic cases, an input at time t_{input} results in a conductance pulse $G(t)$ that is specified as an “alpha function” with a 0.1-ms time-to-rise (t_{rise}), as given by

$$G(t) = G_{max} \frac{(t - t_{input})}{t_{rise}} \exp\{1 - [(t - t_{input})/t_{rise}]\} u(t - t_{input}) \quad (7)$$

In this expression, G_{max} is the amplitude of the pulse, t_{input} is the time of the input pulse, and $u(t)$ represents the unit step (i.e., the Heaviside function). The peak G_{max} of this alpha-function occurs at time t_{rise} after t_{input} .

PERIODIC INPUTS. Periodic inputs are constructed in a manner similar to that described in Reyes et al. (1996). Briefly, discharge times from an input cell are constructed by assuming a periodic train with frequency f and an average discharge rate R (250 spikes/s, independent of f). The stimulus frequency f ranges from 400 to 1,200 Hz. On each period, the probability that an event occurs equals R/f . If an event

occurs during a cycle, it is placed at a fixed phase, i.e., perfectly phase-locked inputs are used. No input refractoriness is included. Three statistically identical and independent input cells are modeled per side. The periodic input trains are 100 ms in duration.

For periodic inputs, each simulation data point (Figs. 5 and 6) represents the average of ten repetitions, which is compatible with the empirical data (Reyes et al. 1996). For cases when the modeled dendritic length varies, it is necessary to vary G_{max} in Eq. 7 to obtain a reliable spike rate (cf. Fig. 6). By contrast, for cases when R_l alone varies (Fig. 5), the conductance amplitude G_{max} for a given input cell is fixed because reliable response rates occur even when R_l changed from 0 to 50 MΩ. For these cases, G_{max} is fixed at 24 nS (30 nS was used in Reyes et al. 1996). This G_{max} value is chosen to match the model response rate from unilateral stimulation with the rate observed empirically in Reyes et al. (1996). For this match, the stimulation frequency is 400 Hz and inputs are applied to the three-compartment model when $R_l = 0$ (the model is a thus a point-neuron).

Analytical and computational methods

For constant conductance inputs, the circuit equations are solved analytically and the relative distribution of the inputs to the two dendrites is explored in terms of the somatic membrane voltage. Analyses are conducted for both compartment-model and cable dendrites. For time-varying inputs, the differential equations (e.g., Eqs. 1–3) are solved numerically. Numerical integration of differential equations is done using a fourth-order Runge–Kutta algorithm with a 5-μs time step. We also tested the effects of using a smaller time step and found results unchanged. Analytical manipulations are conducted with Mathematica (Wolfram Research, Champaign, IL), simulations with the C programming language (Unix and GNU/Linux systems), and plotting with Matlab (The MathWorks, Natick, MA).

RESULTS

Constant-conductance inputs

Constant inputs are used to isolate the effects of spatially distributing inputs to the dendrites from the additional effects that occur with dynamic inputs. We find that dendrites generally enhance the somatic response to bilateral inputs.

SINGLE-COMPARTMENT DENDRITES. Figure 2 shows the somatic potential V_m plotted as a function of the two synaptic conductance inputs, G_1 and G_2 for the three-compartment model shown in Fig. 1C when each dendrite approximates a 150-μm cable. Figure 2A shows a three-dimensional view of the voltage contour and Fig. 2B shows a top view. Two main points are illustrated in these panels. First, the somatic potential V_m monotonically increases with G_1 and with G_2 . Second, V_m saturates as a function of either G_1 or G_2 , with the least saturation when G_1 and G_2 are equal. In fact, the voltage is maximal when G_1 equals G_2 , for a fixed amount of total conductance. This is illustrated by the open circle symbol on the “ $V_m |_{G_1+G_2=150 \text{ nS}}$ ” curve shown in each panel.

Enhancement of balanced bilateral inputs arises from the nonlinear saturating relationship between compartment voltage and conductance input (cf. Koch 1999). For unilateral input of $G_1 = 150$ nS, $G_2 = 0$ in Fig. 2, the values of V_1 , V_2 , and V_m (all with respect to v_d) are 0.834, 0.365, and 0.462, respectively. In contrast, if the same total conductance is delivered in a balanced fashion to both dendrites (i.e., $G_1 = G_2 = 75$ nS), V_1 , V_2 , and V_m are 0.784, 0.784, and 0.603. Because V_m is proportional to the sum of the two dendritic potentials, for the unilateral case, the stimulated dendrite’s potential is nearly saturated (0.834, out of a maximum

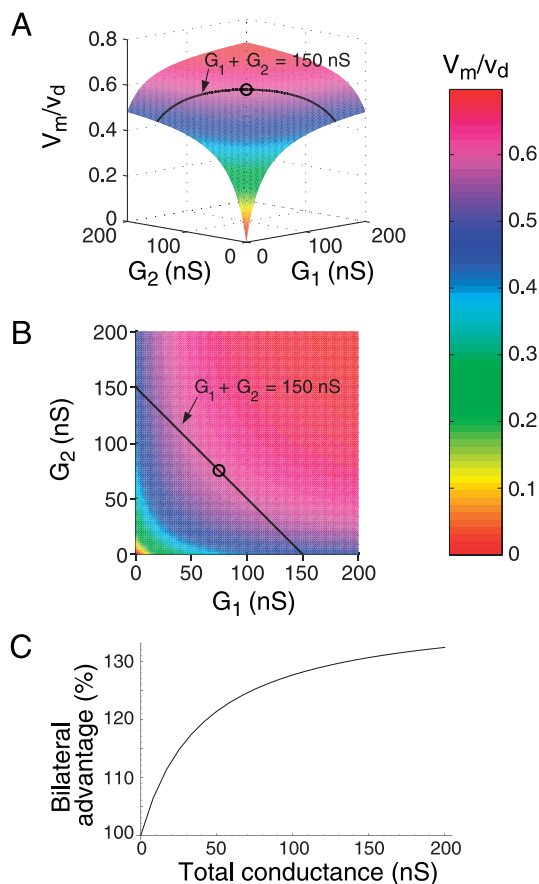


FIG. 2. Voltage contour from constant-conductance inputs. Soma voltage, V_m (divided by v_d), is plotted as a function of G_1 and G_2 [in units of nanosiemens (nS)]. A: 2-dimensional view. B: top view. \circ symbols highlight V_m/v_d when $G_1 = G_2 = 75$ nS. Circuit used to generate this figure is the 3-compartment model shown in Fig. 1C with $R_I = 23.9$ M Ω and $R_D = 90.2$ M Ω , approximating 150- μ m-long 4- μ m dendrites (see METHODS). $R_M = 40$ M Ω . C: "bilateral advantage" is V_m/v_d from balanced bilateral input divided by that from unilateral input, expressed as a percentage. This quantity always exceeds 100% and grows with total conductance.

of 1.0 with infinite conductance input), limiting the resulting somatic potential (0.462). In contrast, for balanced inputs, each dendritic potential is less saturated, but still significant, causing the somatic response to grow to 131% (0.603). Figure 2C plots the somatic response from balanced bilateral input divided by the response with unilateral input as a function of the total input conductance. Enhancement increases monotonically with total conductance but is also significant at lower conductances (e.g., to 121% at 50 nS).

Analytical techniques are used to further elucidate how dendrites enhance bilateral integration. For the three-compartment model (Fig. 1C), the solution for the somatic voltage V_m is given by

$$V_m(G_1, G_2) = v_d \frac{\frac{G_1}{G_1 + \frac{1}{R_D} + \frac{1}{R_I}} + \frac{G_2}{G_2 + \frac{1}{R_D} + \frac{1}{R_I}}}{2 + \frac{R_I}{R_M} - \frac{1}{R_I \left(G_1 + \frac{1}{R_D} + \frac{1}{R_I} \right)} - \frac{1}{R_I \left(G_2 + \frac{1}{R_D} + \frac{1}{R_I} \right)}} \quad (8)$$

Using the preceding equation, we can analytically compare the amount of conductance necessary for a given somatic response between two cases: arbitrary bilateral input from the two sides (i.e., G_1 and G_2), or a single input on one side (i.e., $G_1 = G_s$ and $G_2 = 0$). The corresponding voltage expressions are equated in the following expression

$$V_m(G_1, G_2) = V_m(G_s, 0) \quad (9)$$

For the three-compartment model, Eq. 9 becomes

$$v_d \frac{\frac{G_1}{G_1 + \frac{1}{R_D} + \frac{1}{R_I}} + \frac{G_2}{G_2 + \frac{1}{R_D} + \frac{1}{R_I}}}{2 + \frac{R_I}{R_M} - \frac{1}{R_I \left(G_1 + \frac{1}{R_D} + \frac{1}{R_I} \right)} - \frac{1}{R_I \left(G_2 + \frac{1}{R_D} + \frac{1}{R_I} \right)}} = v_d \frac{\frac{G_s}{G_s + \frac{1}{R_D} + \frac{1}{R_I}}}{2 + \frac{R_I}{R_M} - \frac{1}{R_I \left(G_s + \frac{1}{R_D} + \frac{1}{R_I} \right)} - \frac{1}{R_I \left(\frac{1}{R_D} + \frac{1}{R_I} \right)}} \quad (10)$$

If we clear the fractions and bring all terms to one side, the result can be written as

$$\left[\frac{R_I^2 R_M (R_D + R_I + 2R_M)}{R_D^3} \right] \times [(G_1 + G_2 - G_s)(R_D + R_I)^2 + G_1 G_2 R_D R_I (2(R_D + R_I) + G_s R_D R_I)] = 0. \quad (11)$$

The left-hand side of Eq. 11 is the product of two terms. The first term does not depend on G_1 , G_2 , or G_s . The second term does not depend on R_M . We can solve for G_s in Eq. 11, yielding

$$G_s = \frac{G_1 + G_2 + 2G_1 G_2 \frac{R_D R_I}{R_D + R_I}}{1 - G_1 G_2 \left(\frac{R_D R_I}{R_D + R_I} \right)^2} \quad (12)$$

Equation 12 shows that in the absence of dendrites (i.e., $R_I = 0$), the amount of unilateral conductance G_s needed for a given response equals the sum of the conductances to the two sides under bilateral stimulation ($G_1 + G_2$). However, in the presence of dendrites (i.e., $R_I > 0$), greater unilateral versus bilateral conductance is needed because of the additional additive and subtractive terms in the numerator and denominator respectively of Eq. 12. Thus dendrites enhance bilateral input.

Rearranging Eq. 12 in terms of relative conductances provides an alternative expression of the dendritic advantage as

$$\frac{G_1}{G_s} + \frac{G_2}{G_s} = 1 - \frac{G_1 G_2}{G_s^2} c(2 + c) \quad (13)$$

or

$$\frac{G_2}{G_s} = \frac{1 - \frac{G_1}{G_s}}{1 + c(2 + c) \frac{G_1}{G_s}} \quad (14)$$

where

$$c = \frac{G_s R_D R_I}{R_D + R_I} = G_s (R_D || R_I) \quad (15)$$

Equations 13–15 show that to achieve a given somatic depolarization, less relative conductance from the two sides (i.e., G_1/G_s plus G_2/G_s) is needed compared with that from one side alone. This bilateral advantage occurs whenever the term $c(2 + c)$ is >0 and the extent of this advantage increases with the parameter c , which depends on R_I . Moreover, as shown in Eqs. 11–13, G_1 and G_2 contribute equally to the somatic response, reflecting the symmetry of the model (Fig. 1C). Figure 3 graphically illustrates these effects.

Figure 3 plots the relative conductance combinations that elicit an isosomatic response as given by Eq. 13 or Eq. 14. Three curves are shown, corresponding to three different values of the parameter c . When c is >0 , the total necessary conductance (i.e., $G_1/G_s + G_2/G_s$) required for an isoresponse decreases as G_1 and G_2 become more equal (e.g., see $c = 0.49$ curve when $G_1 = G_2$). As G_1 and G_2 become less equal, in contrast, the total necessary conductance increases monotonically. For larger c , the effect of decreasing the threshold to balanced bilateral input is increased (see “ $c = 2.45$ ” curve). Here, having even a small amount of conductance on one side substantially decreases the required conductance from the other side. For smaller c , in contrast, these effects are decreased (e.g., “ $c = 0.49$ ” curve). In the limiting case when $c = 0$ (corresponding to a point-neuron model), there is no effect of distributing the inputs as indicated by the straight diagonal line. Here, the total conductance required for an isoresponse does not depend on the spatial distribution of inputs because $G_1 + G_2 = G_s$ in Eq. 13 or Eq. 14. In a point-neuron model, $c = 0$ because there is no dendritic length and therefore $R_I = 0$ (see METHODS).

These analyses complement simulations obtained from more complex models. The isoresponse curves in Fig. 3 for c values of 0, 0.49, and 2.45 match the simulations of Agmon-Snir and colleagues (1998; their Fig. 3B) for their no-dendrite (i.e., a single-compartment soma model only), thick-dendrite, and thin-dendrite cases, respectively. In summary, the analysis

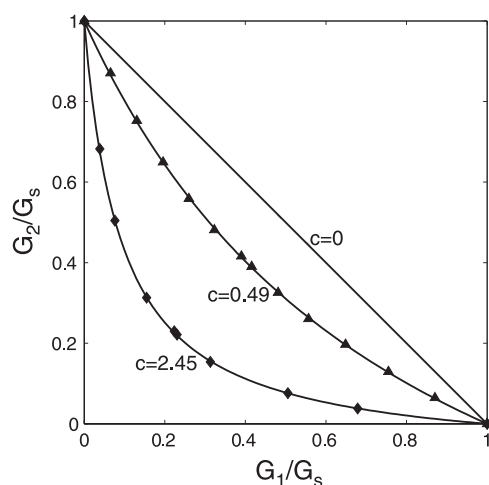


FIG. 3. Analytically derived relative conductance combinations that elicit a constant somatic response (curves), compared with simulation results (symbols) from Agmon-Snir et al. (1998). Response is defined as somatic depolarization in our models (Fig. 1, C–F) and action potential generation in the model proposed by Agmon-Snir et al. (1998). Parameter c is derived in Eqs. 13 to 18 (see RESULTS). $c = 0$ curve (straight line) matches responses that arise from a point-neuron model; $c = 0.49$ and $c = 2.45$ curves match the respective “thick” (triangles) and “thin” (diamonds) dendrites simulations from Agmon-Snir et al. (1998).

using a simple three-compartment model driven by constant conductance inputs shows in the most basic form that dendrites enhance responses to bilateral input.

MULTIPLE-COMPARTMENT DENDRITES. *Conductances at ends.* Using additional analytical approaches, we find that integration of bilateral input is also enhanced in models with multiple compartment dendrites, including cables dendrites. Voltage contours (not shown) are maximal when a given amount of conductance is distributed equally to the two dendrites in multicompartment models, like those arising from single-compartment dendrites (e.g., Fig. 2). When analyses to find the conductance distribution that elicits a somatic isoresponse are repeated with multiple-compartment dendrites, identical expressions to Eq. 13 or Eq. 14 arise, with c depending on the number of dendritic compartments. As the number of dendritic compartments increases, c expressions grow in complexity, but still depend only on combinations of R_I and R_D that are scaled by G_s . This analytical result holds for all numbers of compartments because it occurs for the general five-compartment model shown in Fig. 1F, where R_b , R_c , and R_e are arbitrary resistances (assume for the moment that R_d is infinite). For this model, c is made up of a combination of R_b , R_c , and R_e , scaled by G_s . Because any multicompartment dendritic model, regardless of the number of compartments, can be reduced to such a circuit through the use of delta-to-Y conversions, the analytic result holds for all cases.

For an infinite number of compartments, each dendrite becomes a finite-length cable (Fig. 1E when $X = 0$). Here, c can be expressed in terms of the electrotonic length L of the cable and the input resistance of an infinite-length cable with similar properties (see METHODS) as

$$c = G_s R_\infty \tanh(L) \quad (16)$$

In terms of basic cable parameters (l , d , R_i , and R_d), c in Eq. 16 is

$$c = G_s \frac{2\sqrt{R_i R_d}}{\pi d^{3/2}} \tanh\left(2l \sqrt{\frac{R_i}{d R_d}}\right) \quad (17)$$

Equations 16 and 17 (derived in the APPENDIX) together with Eqs. 13 and 14 demonstrate analytically that the dendritic enhancement increases with dendritic length because the hyperbolic tangent function increases monotonically with l . Because of the inverse dependency on d in Eq. 17, dendritic enhancement also increases for thinner dendrites.

Considering again dendrites with a finite number of compartments, the bilateral enhancement increases with the number of compartments when a dendritic cable with a fixed size and electrical properties is assumed (see METHODS). When c values are compared for such cases [e.g., Fig. 1D (two dendritic compartments) vs. Fig. 1C (one compartment)], the resulting c values (divided by G_s) increase monotonically with the number of compartments to an upper asymptote given by the continuous cable.¹ Thus the three (total) compartment

¹ For the comparison between different finite numbers of dendritic compartments, the enhancement was analytically larger for greater numbers of compartments: one to five, eight, and 12 compartments per dendritic section were compared. For the comparison between compartment-model and cable dendrites, standard values for the specific axial resistivity R_i , dendritic resistance R_d , and dendritic diameter d were assumed (see METHODS); the largest enhancement occurred with cable dendrites across all dendritic lengths l .

model in Fig. 1C represents a lower bound for the amount of bilateral stimulation advantage.

Conductances in interior compartments. If inputs are placed symmetrically at an interior dendritic compartment (of a multicompartment dendritic model) or an interior position of a dendritic cable, bilateral enhancement can also be shown analytically. This is because the result from the general five-compartment model shown in Fig. 1F holds for arbitrary R_a , including finite values that occur with interior inputs. For the cable model with interior inputs shown in Fig. 1E, c is given by

$$c = G_s R_s \frac{\cosh(X) \sinh(L-X)}{\cosh(L)} \quad (18)$$

where X is the electrotonic distance of the input placement from the ends of the dendrite. X therefore ranges between 0 and L . Based on Eq. 18, c is maximal when inputs are placed at the ends of the dendrites (i.e., when $X = 0$) and c decreases monotonically as the inputs are placed closer to the soma (i.e., as $X \rightarrow L$).

Distributed conductances. We also tested the effects of distributing inputs spatially along the length of multicompartment dendrites. For these cases, a simple form like Eq. 13 is not achievable. This is because no terms that contain R_M and exclude G_1 , G_2 , and G_s (and vice versa) can be factored as was done with isolated input placement (e.g., Eq. 11). Even though a similar analytical expression is not found when inputs are distributed all along the dendrites, enhancement to balanced bilateral stimulation does occur for these cases. Voltage contours (not shown) were computed for both the five- (Fig. 1D) and seven-compartment (not shown) models. For these cases, the somatic voltage response as a function of G_1 and G_2 is largest when a fixed amount of conductance is distributed equally to both sides and the response monotonically decreases as the conductance distribution is increasingly imbalanced to the two sides, consistent with responses obtained when inputs are delivered to an isolated compartment (e.g., Fig. 2). Thus dendritic enhancement of bilateral input occurs when inputs are either spatially confined or when they are distributed along the length of dendrites.

In summary, analyses using constant conductance inputs show that the bipolar dendritic structure of coincidence detector cells enhances the somatic response to bilateral inputs. This enhancement increases with dendritic length, thinness, and number of compartments as given by the factor c . Dynamic inputs are used in the rest of this study to explore the effects of dendritic length on ITD sensitivity. We restrict attention to the three-compartment model because this case provides a lower bound on the amount of bilateral stimulation advantage.

Paired-pulse inputs

In this section, dynamic stimuli are used to investigate how dendritic length and the spatial distribution of inputs affect coincidence sensitivity. The primary results are shown in Fig. 4. Isolated pairs of equal-amplitude, transient-conductance pulses (Fig. 4A) are delivered to the dendrites of the three-compartment model shown in Fig. 1B. The time delay τ between the pulses is varied. Inputs are applied in two different spatial configurations: both pulses delivered to the same dendrite (dashed lines) and each pulse delivered to a distinct

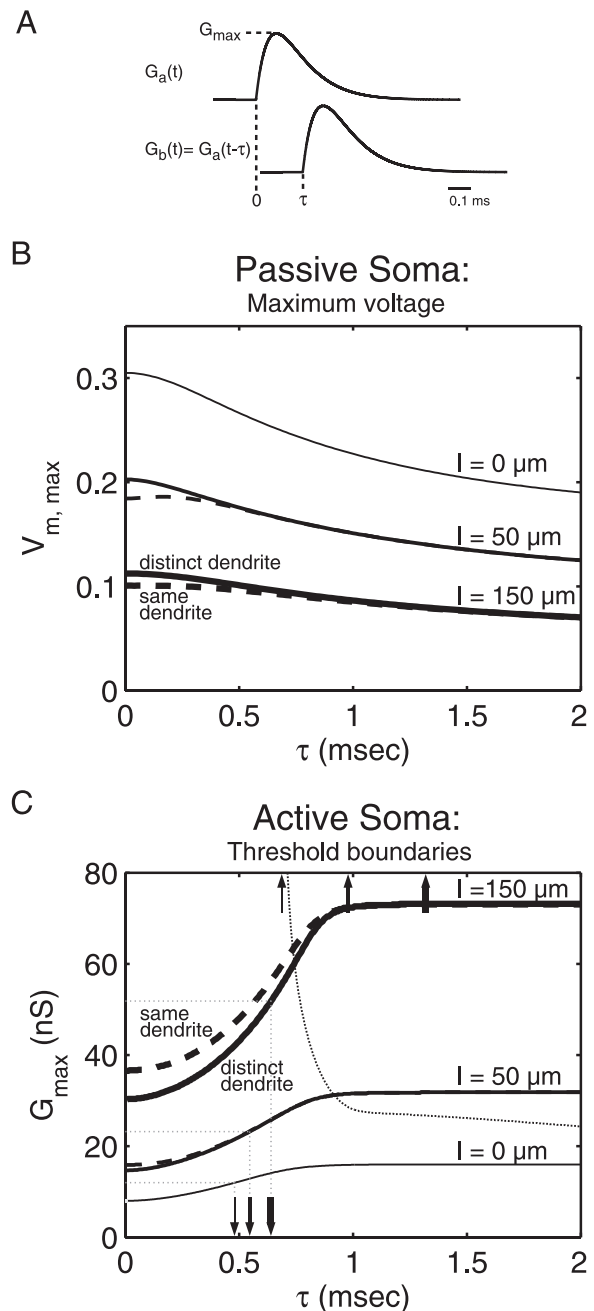


FIG. 4. *A*: pairs of transient conductance pulses applied to the 3-compartment model (Fig. 1B). *B*: responses with passive soma. *C*: responses with active soma. In *B* and *C*, both dendritic length, l , and the dendritic location of stimulation are parameters. "Same dendrite" means [$G_1 = G_a(t) + G_b(t)$, $G_2 = 0$], whereas "distinct dendrite" means [$G_1 = G_a(t)$, $G_2 = G_b(t)$]. In *B*, the maximum value of the normalized soma voltage ($\max[V_m(t)/v_d]$) is plotted as a function of interpulse delay τ . $G_{max} = 24$ nS in this panel. *C*: plot of the minimum conductance boundaries required for an action potential. Points above a given curve generate an action potential; points below do not. Both G_{max} and τ are varied. Also plotted in *C* are the halfwidths of coincidence windows (down arrows) and the absolute refractory periods (up arrows), as a function of dendritic length for distinct dendrite stimulation. Additional thin dotted boundary shown in *C* separates 1 and 2 action potentials for the $l = 0$ case.

dendrite (solid lines). Responses for passive and active somata are shown in Fig. 4, *B* and *C*, respectively.

PASSIVE SOMA. Normalized maximal voltage response is plotted as a function of interpulse delay in Fig. 4B. The amplitude

of the conductance pulse is fixed for this panel ($G_{max} = 24$ nS in Eq. 7). Similar responses (not shown) occur for other values of G_{max} . As the time delay between the pulses increases, the maximal response decreases, consistent with typical coincidence detection behavior observed in NL and MSO cells (e.g., Funabiki et al. 1998; Grothe and Sanes 1994; Joseph and Hyson 1993). Model response also generally decreases as dendritic length l increases as a consequence of greater voltage attenuation at the soma (see cases, in order, $l = 0, 50,$ and $150 \mu\text{m}$).

The spatial distribution of inputs systematically affects responses. When each pulse is delivered to a unique dendrite, the response is always greater than or equal to the response when both pulses are delivered to the same dendrite (Fig. 4B, solid vs. dashed lines). A larger response to distinct (i.e., bilateral) versus same (i.e., monolateral) dendritic stimulation is consistent with the findings using constant-conductance inputs showing that the largest somatic response occurs when a fixed amount of conductance is distributed equally to the two dendrites (e.g., Fig. 2). The enhanced response to bilateral inputs is most pronounced at the smallest interpulse delays and decreases with delay (Fig. 4B). At the longest delays, the response is the same whether the inputs are distributed bilaterally or unilaterally, as expected, and evidenced by the similarity of the associated solid and dashed curves. Similar responses (not shown) occur when rectangularly shaped conductance pulses are used.

ACTIVE SOMA. For an active soma, Fig. 4C shows the minimum conductance required to stimulate action potentials as a function of delay. Here, both the interpulse delay (τ , abscissa) and the amplitude of each conductance pulse (G_{max} , ordinate) are varied and the boundaries that separate a somatic response (i.e., the presence of an action potential) from no-response (i.e., no action potential) are plotted for the same six conditions tested in Fig. 4B. The resulting boundaries indicate that to elicit a somatic response, less conductance is needed at the smallest delays and progressively more conductance is necessary as interpulse delay increases. Along the curved region of a given boundary, the model cell acts like a coincidence detector because the model response depends on the delay between the pulses. In contrast, for large delays, larger-amplitude conductance pulses elicit a response to the first pulse in isolation. Here, the boundaries are flat, indicating that the cell is insensitive to the time delay between the two input pulses.

Distributing inputs to either the same dendrite or distinct dendrites yields a different boundary region, with less conductance required for distinct dendritic stimulation (Fig. 4C, solid vs. dashed curves). A decreased conductance threshold for distinct dendritic stimulation is consistent with the minimal total conductance necessary for bilaterally balanced constant inputs (Fig. 3). As seen in Fig. 4C, the difference between the same and distinct dendritic stimulation boundaries is larger at smaller delays and decreases with delay, consistent with passive soma responses (e.g., Fig. 4B).

Longer dendrites, moreover, increase the difference between bilateral and unilateral stimulation (compare curve $l = 150 \mu\text{m}$ with curve $l = 50 \mu\text{m}$). This bilateral enhancement with dendritic length is consistent with the constant-input analyses showing that the parameter c , which also depends on dendritic length, increases the bilateral stimulation advantage (Fig. 3). Figure 4C also shows that the half-width of the coincidence

window (up arrows) and the absolute refractory period (down arrows) both increase with dendritic length. The additional thin dotted black curve shows the boundary separating one and two action potentials for the $l = 0$ case. As G_{max} increases, this boundary approaches an asymptotic time delay indicated by the corresponding up arrow, which is the absolute refractory period. (For clarity, only up arrows reflecting the refractory periods for the cases $l = 50 \mu\text{m}$ and $l = 150 \mu\text{m}$ are shown, not the boundaries separating one and two action potentials.) In summary, dendrites enhance coincidence sensitivity to pulsatile input and this enhancement increases with dendritic length.

Periodic inputs: rate-ITD modulation

Model ITD sensitivity to periodic input trains is reported in this section. The same three-compartment cell model with active soma is used as in Fig. 4C, together with a periodic input model from Reyes et al. (1996) as described in METHODS. Simulations are computed for two cases: first, where R_l alone varies (values of 0, 20, and 50 M Ω are tested); and second, where dendritic length varies (the same values are used as in Fig. 4). The effect of stimulus frequency f is examined for both cases. In contrast to the results presented thus far, which used deterministic inputs and deterministic cell responses, there is now randomness in the input patterns, causing stochastic responses. Also, in this section, inputs from each side always innervate a distinct dendrite.

R_l VARIES. Empirical and model results are shown in Fig. 5. In vitro data from Reyes et al. (1996) are shown in Fig. 5A and model results are shown in Fig. 5, B–D, with each panel representing a different R_l value. Responses in Fig. 5 are

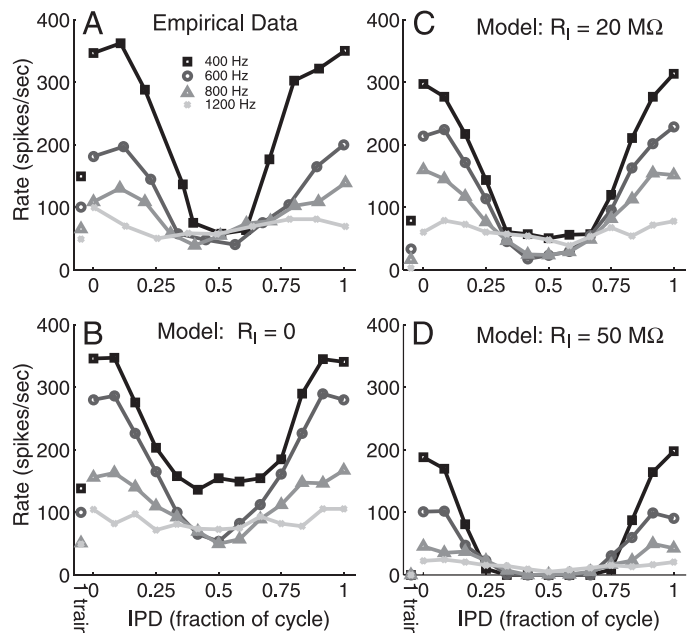


FIG. 5. Rate-IPD curves from in vitro data (A) and 3 model cases where R_l varies (B–D). In all panels, response rate is plotted as a function of IPD, where IPD = interaural time difference (ITD) $\times f$. Stimulus frequency f is varied as a parameter. Data in A are from Reyes et al. (1996; their Fig. 8A). Cell model is the same 3-compartment model used in Fig. 4C. Periodic input trains are constructed in a manner similar to that in Reyes et al. (1996), see METHODS. “1 train” indicates stimulation when input from one side is delivered to one dendrite only—no input is delivered to the other side.

plotted on a common interaural phase difference (IPD) axis, where $IPD = ITD \times f$. This transformation aids the comparison across frequency. Model results are consistent with the empirical data showing that rate and rate-IPD modulation (i.e., the amount of change in rate as IPD varies) decrease as stimulation frequency increases. The modeling simulations additionally show a diversity in response that depends on the degree of dendrite-to-soma coupling (G_{max}). Model response rate at out-of-phase (or "anticoincident") delays is reduced sharply at low frequencies with increasing compartmental separation (observe the 400- and 600-Hz curves across *B-D*, respectively). These findings are consistent with simulations from Agmon-Snir et al. (1998), where out-of-phase rates were reduced for thinner dendrite cases compared with either thicker dendrite or point-model cases. Our findings are also consistent with those of Grau-Serrat et al. (2003), where maximal rate-IPD modulation was found with low-frequency stimulation and modulation generally decreased with stimulus frequency. In both the empirical data (*A*) and our model (*B-D*), little modulation is observed at high frequencies (e.g., 1,200 Hz).

DENDRITIC LENGTH VARIES. Figure 6 shows the effects of dendritic inclusion and conductance level on rate-IPD responses. Figure 6, *A-D* illustrates the effects of dendritic length and stimulation frequency with G_{max} as a parameter. To more easily express the magnitude of modulation, only two points along the rate-IPD curve, the coincident rate (i.e., when $IPD = 0$) and the anticoincident rate (i.e., when $IPD = 0.5$), are further examined (e.g., Dasika et al. 2005). Figure 6*E* plots the data from *A-D* in (coincident rate, anticoincident rate) space like that in Agmon-Snir et al. (1998). Here, maximum modulation would be represented by a horizontal line along the

x -axis, reflecting a coincident rate that is greater than zero and an anticoincident rate that equals zero.

Response rate generally increases with conductance level (Fig. 6, *A-D*) and decreases with dendritic length (compare *B* with *A* and *D* with *C*). Greater rate-IPD modulation occurs at 400 versus 1,200 Hz, consistent with empirical data (Reyes et al. 1996). Moreover, because response rates decrease with dendritic length, G_{max} was specified to vary (e.g., Agmon-Snir et al. 1998). Two main results are seen in Fig. 6 beyond those expected from typical coincidence detection behavior. First, unilateral rates can be higher than bilateral rates in models with passive dendrites (cf. *B* and *D*, $G_{max} = 200$ and 300 nS). These findings show that the response from inputs to just one side (i.e., "1 train" response) can actually exceed the response from bilateral inputs in a model with passive dendrites, like that seen in the Grau-Serrat et al. (2003) model that specified active dendrites. Second, passive dendrites improve modulation at 400 Hz (*E*, solid thick vs. solid thin curve), but have less effect at 1,200 Hz as evidenced by the greater similarity between the thick and thin dotted curves. In fact, at 1,200 Hz, no dendrites provide slightly more modulation than the 150- μ m-length dendrites because the thin dotted curve is generally closer than the thick dotted curve to the x -axis. In summary, the three-compartment model with periodic inputs can account for the frequency dependency observed in empirical data, as well as nonlinear response-rate trends and the relationship between dendritic length and stimulus frequency observed in more complex models.

DISCUSSION

This paper explores the effects of dendrites in simplified, single-neuron models of auditory coincidence-detector cells. A

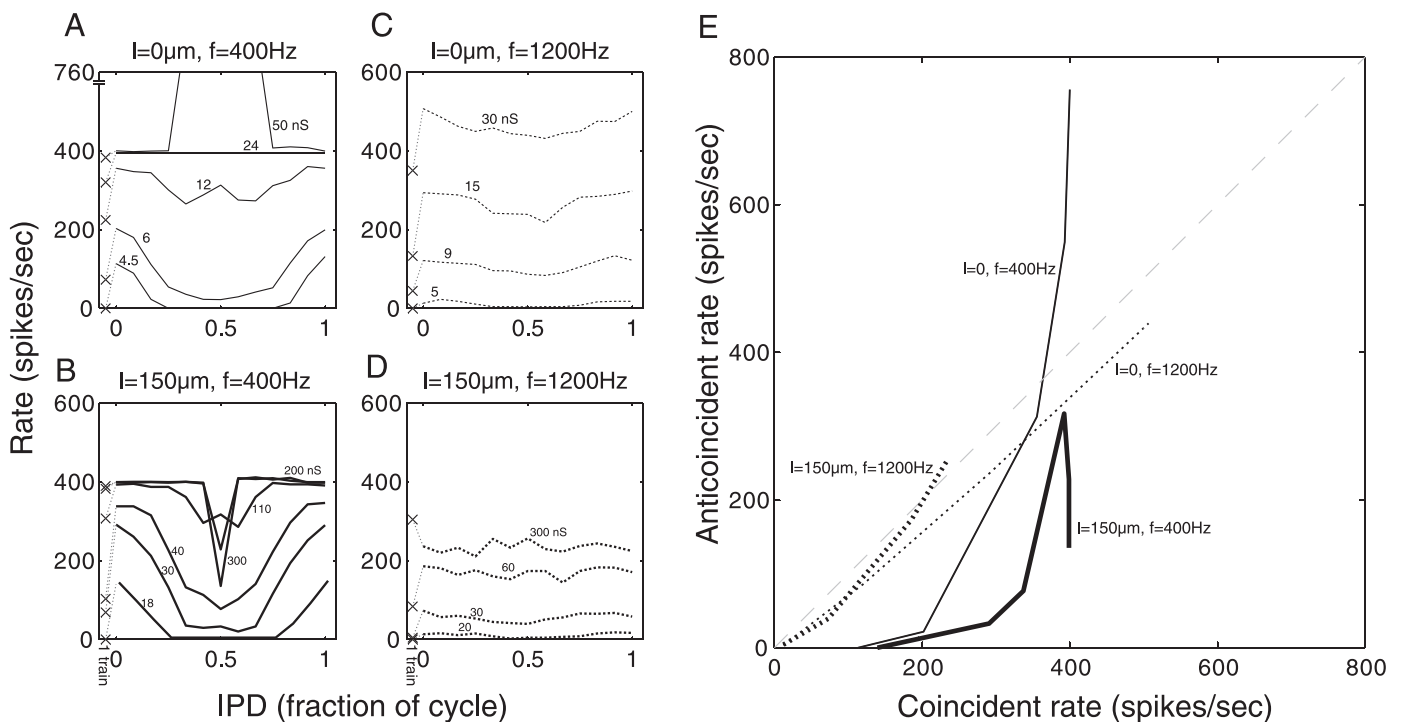


FIG. 6. Model rate-IPD curves when dendritic length, l , frequency, f , and G_{max} vary. *A-D*: follow the same format as in Fig. 5 (the same 3-compartment model is used as in Fig. 4C). Parameter is G_{max} . \times symbols indicate the unilateral response rate for the associated G_{max} curve. *E*: data plotted in (coincident rate, anticoincident rate) space. Thin gray dashed line with unity slope indicates no rate-IPD modulation (i.e., coincident rate equals anticoincident rate).

model cell is composed of a single-compartment soma with two passive dendritic sections, each section consisting of a compartment model or a cable. Excitatory inputs are delivered to the dendrites as conductance changes that depolarize the soma. Using a combination of analytical and computational techniques, we demonstrate that the inherent bipolar dendritic structure of NL and MSO cells enhances binaural integration and coincidence detection. Although binaural cells are the focus, our results suggest that dendrites generally enhance coincidence detection in neurons across the nervous system.

Dendrites enhance bilateral integration

The dendritic enhancement of bilateral input is a time-independent phenomenon that depends systematically on model and input parameters. Using a variety of simple models with constant inputs (e.g., Fig. 1, *C–F*), we demonstrate analytically that balanced bilateral stimulation to the two dendrites elicits the largest somatic response (e.g., Fig. 2) and requires the least conductance for an isosomatic response (Fig. 3, *Eqs. 13–18*). The total conductance necessary for an isoresponse monotonically increases as the input distribution becomes increasingly imbalanced to the two dendrites (Fig. 3, *Eqs. 13–18*). This “bilateral advantage” occurs regardless of whether each dendrite is made up of a single compartment (*Eqs. 13–15*), a finite number of multiple compartments (e.g., *Eqs. 13* and *14*), or a cable (*Eqs. 13, 14, 16–18*). The magnitude of the bilateral advantage depends on a single parameter c (Fig. 3), which depends on R_D and R_I for compartment model dendrites (e.g., *Eq. 15*) and on dendritic length, diameter, and the specific cable parameters for cable dendrites (*Eqs. 16–18*). Moreover, for models with a finite number of compartments that approximate a dendritic cable with a fixed size, the bilateral advantage increases with the number of model compartments. Thus the model with single-compartment dendrites, or three total model compartments in Fig. 1*C*, provides a lower bound for the amount of advantage to bilateral input.

Our analyses provide insight into the results Agmon-Snir and colleagues (1998) obtained using more detailed models. Their simulations used a multicompartment cell model consisting of one soma compartment with active ion channels, two four-compartment dendritic sections, and a multicompartment axon. The dendrites were stimulated by periodic input trains of jittered, transient conductance pulses. Somatic response was defined as a propagated axonal action potential. Our isoresponse curves for c values of 0, 0.49, and 2.45 (Fig. 3) match the simulation results from Agmon-Snir and colleagues (1998; their Fig. 3*B*) corresponding to adendritic (i.e., a single-compartment soma only), thick-dendrite, and thin-dendrite cases, respectively. Thus any passive dendritic model with constant inputs, including the minimal three-compartment model (Fig. 1*C*), predicts the isoresponse properties from a much more complex model that has both spatial and temporal factors affecting the response.

The mechanism underlying the bilateral dendritic stimulation enhancement is the saturating, sublinear relationship between input conductance and compartment voltage (cf. Koch 1999). This effect is seen most easily in the steady state when constant inputs drive the three-compartment model (Fig. 1*C*). When inputs from the two sides are equally segregated on bipolar dendrites, the resulting currents from the inputs com-

bine almost linearly (because the voltage of each dendritic compartment is less saturated). The response in Fig. 2, *A* and *B* when G_1 and G_2 are equal illustrates this more-linear integration. Interaction, however, becomes more sublinear as the input distribution to the two dendrites is increasingly imbalanced (because the voltage of the more weighted dendrite becomes more saturated). In the limit, when inputs are distributed unilaterally, they combine most sublinearly as a consequence of greatest voltage saturation (Agmon-Snir et al. 1998; Rall 1964, 1970; Segev 1998). The response shown in Fig. 2 when either G_1 (or G_2) is zero, illustrates this limiting sublinear saturation. The enhancement to balanced bilateral inputs, moreover, increases with either longer or thinner dendrites (*Eqs. 15* and *16*) or when inputs are placed closer to the ends of the dendrites (*Eq. 18*) because the two dendrites become less coupled (cf. Fig. 3 as c increases). Enhancement also increases with the total input conductance (Fig. 2*C*, *Eqs. 15–18*).

A further simplification of the model would be to use current sources as inputs instead of conductances. In this case, the relationship between applied current and compartment voltage is always linear. Consequently, there would be no difference when inputs are distributed in different configurations to the dendrites, regardless of input strength. Thus the three-compartment model with conductance inputs represents the simplest model that embodies bilateral enhancement.

Dendrites improve coincidence detection

The binaural enhancement demonstrated with constant inputs extends to the coincidence detection of (time-varying) inputs (Fig. 4). Cells with longer dendrites are more sensitive to bilateral versus unilateral coincidences (Fig. 4*C*), consistent with the reduced total conductance necessary to achieve a given somatic response to balanced, constant inputs (Fig. 3).

IMPLICATIONS FOR DENDRITIC LENGTH GRADIENT. Our coincidence detection results suggest three reasons for a functional role for the dendritic length gradient in NL, where low-CF cells have long dendrites. First, longer dendrites require stronger net bilateral inputs to achieve soma response (cf. Fig. 4*C*, compare curves $l = 150, 50,$ and $0 \mu\text{m}$). Stronger input per sound cycle is expected from low- versus high-frequency nucleus magnocellularis (NM) cells. Multiple frequency-tuned NM cells from the two sides excite a single NL cell (e.g., Carr and Boudreau 1993). A greater proportion of low- versus high-frequency NM cells will discharge synchronously in the same period as a result of the physiologically observed constant average firing rate across frequency (e.g., Warchol and Dallos 1990). This would cause a stronger effective input per stimulus cycle, given similar synaptic properties across frequency. Second, models with longer dendrites have wider (i.e., extending further in ITD) coincidence windows (Fig. 4*C*, down arrows), which are better suited for the long periods arising from low-frequency inputs. Third, the absolute refractory period increases with dendritic length (cf. Fig. 4*C*, up arrows). A larger refractory period would decrease the possibility that NL would have two firings in the same sound cycle at the least-coincident delays at low frequencies, which would otherwise degrade coincidence detection (e.g., Fig. 6*A* “50 ns” vs. Fig. 6*B* “300 ns”). Low-frequency inputs thus appear suited to take advantage of the increased dynamic range for coincidence

detection afforded by long dendrites. High-frequency inputs, conversely, do not appear suited for cells with long dendrites. The periods of high-frequency inputs are small and the inputs are weak (assuming less synchronization). Consequently, cells with short dendrites appear better suited to process high-frequency inputs (e.g., Fig. 4C, $l = 0$ curve). Our simulations with periodic inputs are in agreement with the observed length gradient in NL because maximal rate-ITD modulation occurs at low frequencies in models with dendrites and at high frequencies in models without dendrites (Fig. 6E).

COINCIDENCE DETECTION OF PERIODIC INPUTS. The model responses to periodic inputs (Figs. 5 and 6) are consistent with both in vitro responses and those arising from more realistic models. Coincidence detection of low-frequency inputs improves with longer dendrites (Fig. 6E), consistent with more complex models (Agmon-Snir et al. 1998; Grau-Serrat et al. 2003), and was robust across a tenfold-plus range of input conductance (Fig. 6, B and E). Less coincidence sensitivity occurred at high frequencies, consistent with empirical data (Reyes et al. 1996; Fig. 5A), even with negligible dendrites (Figs. 5B and 6, C and E). Moreover, the model simulations predict the nonlinear property that the response to input from just one side, without any spontaneous activity on the other side, can exceed that from two-sided stimulation (Fig. 6, B and D, 300-nS cases). Grau-Serrat and colleagues (2003) demonstrated this phenomenon with a biophysically detailed model of NL that had active dendrites. Our results suggest that a three-compartment model with passive dendrites and an active soma constitutes the minimal model that can embody this nonlinearity.

Other models show that rate-ITD modulation can be influenced by active channels and by an asymmetrical cell morphology. For example, inclusion of low-threshold potassium channels in models was previously demonstrated to increase coincidence sensitivity (Grau-Serrat et al. 2003; Svirskis et al. 2003, 2004). Furthermore, empirical data show that an increase in the density of low-threshold potassium conductance is correlated with the heightened coincidence sensitivity of middle-CF NL cells (Kuba et al. 2005). Future models could vary dendritic length while incorporating the empirically observed tonotopic variations in potassium channel density and examine consequent effects on coincidence sensitivity. Asymmetrical cell models could also be tested. MSO cells with axons that are offset from the soma were observed empirically (Smith 1995; cf. Fig. 1A, this paper). Asymmetrical axonal placement was demonstrated computationally to influence coincidence detection (Brew 1998; Zhou et al. 2005).

Finally, inhibitory inputs, which innervate MSO and NL, could enhance dendritic processing. Empirical data and models show that inhibition reduces the excitability of coincidence detector cells, which can improve coincidence sensitivity (e.g., Dasika et al. 2005; Grothe and Sanes 1994; Yang et al. 1999). To reach voltage spiking threshold in the presence of inhibition, greater conductance is required. In dendritic cells, greater conductance enhances bilateral integration (Fig. 2C, Eqs. 15–18) and improves coincidence detection (Fig. 4C). Inhibition and dendritic processing could thus be acting synergistically to enhance binaural processing. This may be especially important for high-frequency NL cells where inhibition could effectively “lengthen” dendrites that are physically short. Further, at least

some degree of inhibitory enhancement of dendritic coincidence detection is expected despite variations in the temporal synchrony (i.e., phase-locking) and synaptic kinetics (i.e., time constant) of the inhibitory input. Consequently, enhancement should be present in both the avian system, which has unsynchronized, slow inhibition (e.g., Yang et al. 1999), and the mammalian system, which has phase-locked, faster inhibition (e.g., Brand et al. 2002; for review see Grothe 2003).

In conclusion, dendritic enhancement of coincidence detection is a general phenomenon that arises from the spatial separation of conductance inputs to distinct, passive dendrites. The somatic response is enhanced because each dendrite’s response is recruited in a more linear, balanced manner compared with a more saturated, imbalanced manner. Enhancement occurs in both cable and compartmental dendritic models, with passive or active somata, with as few as three (total) compartments. The extent of improvement, moreover, analytically depends on the dendritic parameters. Longer, thinner dendrites and greater numbers of dendritic compartments increase the dendritic advantage. Improvement occurs when inputs are spatially isolated or distributed along the length of multiple-compartment dendrites. The time-independent enhancement of balanced inputs underlies the improved coincidence detection of time-varying input. As the stimulation frequency of periodic inputs increases, coincidence detection degrades, consistent with empirical data. Longer dendrites improve and maintain robust coincidence detection at low frequencies, implicating a functional role for the observed dendritic length gradient. Our study provides an example of how the combination of analytical and computational modeling can elucidate neural mechanisms that improve information processing.

APPENDIX

The solution of Eqs. 14 and 16 is given for the cable dendrites model shown in Fig. 1E, first for the case with inputs at the dendrite ends ($X = 0$). To derive $V_m(G_1, G_2)$, we use superposition

$$V_m(G_1, G_2) = V_m(G_1, G_2)|_{\text{left } v_d=0} + V_m(G_1, G_2)|_{\text{right } v_d=0} \quad (\text{A1})$$

To find $V_m(G_1, G_2)|_{\text{left } v_d=0}$, we first find the input resistance into the left dendritic section using Eq. 5 (see METHODS). We define R_{eq1} as the parallel combination of this input resistance and the somatic resistance R_M . Equation 5 is used again to find the input resistance (R_{eq2}) looking from G_2 into the right-side cable terminated by the equivalent resistance R_{eq1} . The voltage $V(0)$ at the proximal end (i.e., right side) of this cable is $v_d G_2 R_{eq2} / (G_2 R_{eq2} + 1)$. The solution for $V_m(G_1, G_2)|_{\text{left } v_d=0}$ is then given by $V(L)$ in Eq. 4 for the cable terminated with R_{eq1} .

Based on symmetry, $V_m(G_1, G_2)|_{\text{right } v_d=0}$ is simply $V_m(G_1, G_2)|_{\text{left } v_d=0}$ with G_1 and G_2 interchanged. After combining and simplifying expressions, the (total) somatic voltage $V_m(G_1, G_2)$ can be written as

$$\begin{aligned} V_m(G_1, G_2) = & v_d 2R_s R_M (G_1 + G_2) \cosh [L] + 2G_1 G_2 R_s \sinh [L] / \\ & [R_s (1 + \cosh (2L)) + 2R_M \sinh (2L) \\ & + (G_1 + G_2) R_s [2R_M \cosh (2L) \\ & + R_s \sinh (2L)] + G_1 G_2 R_s^2 \{ R_s [\cosh (2L) - 1] + 2R_M \sinh (2L) \}] \quad (\text{A2}) \end{aligned}$$

From Eq. A2, the cable analogue of the three-compartment model Eqs. 9–12 can be found, yielding identical Eqs. 13 and 14, and the c expression for cable dendrites given by Eq. 16.

The solution of $V_m(G_1, G_2)$ given symmetrical interior placement of inputs is found using similar methods. Here, each dendritic section is modeled as two cable sections, with the input between the two sections (Fig. 1E when $X \neq 0$). Using similar analyses, Eqs. 13, 14, and 18 are found.

ACKNOWLEDGMENTS

We thank Drs. Laurel Carney, Bob Dizon, and Steve Bierer for helpful comments on earlier versions of this manuscript. We extend special thanks to the two reviewers and Dr. Catherine Carr whose comments greatly improved this paper. The suggestions to include cable analysis and to better connect the cable and compartmental models were especially helpful.

GRANTS

This work was supported by National Institutes of Health Grants R01 DC-00100, R01 NS-34425, and 5 T32 DC-000018.

Present address of V. Dasika: Virginia Merrill Bloedel Hearing Research Center, University of Washington, Box 357923, Seattle, WA 98195-7923.

REFERENCES

- Agmon-Snir H, Carr CE, Rinzel J. The role of dendrites in auditory coincidence detection. *Nature* 393: 268–272, 1998.
- Archie KA, Mel BW. A model for intradendritic computation of binocular disparity. *Nat Neurosci* 3: 54–63, 2000.
- Boord RL. Ascending projections of the primary cochlear nuclei and nucleus laminaris in the pigeon. *J Comp Neurol* 133: 523–541, 1968.
- Brand A, Behrend O, Marquardt T, McAlpine D, Grothe B. Precise inhibition is essential for microsecond interaural time difference coding. *Nature* 30: 543–547, 2002.
- Brew HM. Modeling of interaural time difference detection by neurons of mammalian superior olivary nucleus. *Assoc Res Otolaryngol Abstr* 25: 680, 1998.
- Brown CH. Sound localization. In: *Comparative Hearing: Mammals*. New York: Springer-Verlag, 1994, vol. 4.
- Carr CE, Boudreau RE. Organization of the nucleus magnocellularis and the nucleus laminaris in the barn owl: encoding and measuring interaural time differences. *J Comp Neurol* 334: 337–355, 1993.
- Dasika VK, White JA, Carney LH, Colburn HS. Effects of inhibitory feedback in a network model of avian brain stem. *J Neurophysiol* 94: 400–414, 2005.
- Durlach NI, Colburn HS. Binaural phenomena. In: *Handbook of Perception*. New York: Academic Press, 1978, vol. 4.
- Funabiki K, Koyano K, Ohmori H. The role of GABAergic inputs for coincidence detection in the neurons of nucleus laminaris of the chick. *J Physiol* 508: 851–869, 1998.
- Grau-Serrat V, Carr CE, Simon JZ. Modeling coincidence detection in nucleus laminaris. *Biol Cybern* 89: 388–396, 2003.
- Grothe B. New roles for synaptic inhibition in sound localization. *Nat Rev Neurosci* 4: 540–550, 2003.
- Grothe B, Sanes DH. Synaptic inhibition influences the temporal coding properties of medial superior olivary neurons: an in vitro study. *J Neurosci* 14: 1701–1709, 1994.
- Jeffress LA. A place theory of sound localization. *J Comp Physiol Psych* 41: 35–39, 1948.
- Joris PX, Smith PH, Yin TC. Coincidence detection in the auditory system: 50 years after Jeffress. *Neuron* 21: 1235–1238, 1998.
- Joseph AW, Hyson RL. Coincidence detection by binaural neurons in the chick brain stem. *J Neurophysiol* 69: 1197–1211, 1993.
- Koch C. *Biophysics of Computation. Information Processing in Single Neurons*. New York: Oxford Univ. Press, p. 19–37, 1999.
- Kuba H, Yamada R, Fukui I, Ohmori H. Tonotopic specialization of auditory coincidence detection in nucleus laminaris of the chick. *J Neurosci* 25: 1924–1934, 2005.
- MacLeod KM, Soares D, Carr CE. Interaural timing difference circuits in the auditory brainstem of the emu (*Dromaius novaehollandiae*). *J Comp Neurol* 495: 185–201, 2006.
- Parks TN, Rubel EW. Organization and development of brain stem auditory nuclei of the chicken: organization of projections from n. magnocellularis to n. laminaris. *J Comp Neurol* 164: 435–448, 1975.
- Pinsky PF, Rinzel J. Intrinsic and network rhythmogenesis in a reduced Traub model for CA3 neurons. *J Comput Neurosci* 1: 39–60, 1994.
- Rall W. Cable properties of dendrites and effects of synaptic location. In: *Excitatory Synaptic Mechanisms*, edited by Anderson P, Jansen JKS. Oslo, Norway: Universitetsforlaget, 1970, p. 175–187.
- Rall W. Theoretical significance of dendritic trees for neuronal input–output relations (1964). In: *The Theoretical Foundation of Dendritic Function: Selected Papers of Wilfrid Rall with Commentaries*, edited by Segev I, Rinzel J, Shephard G. Cambridge, MA: The MIT Press, 1995, p. 122–146.
- Ramón y Cajal S. Les ganglions terminaux du nerf acoustique des oiseaux [in French]. *Trab Lab Invest Biol Univ Madrid* 6: 195–225, 1908.
- Reyes AD, Rubel EW, Spain WJ. In vitro analysis of optimal stimuli for phase-locking and time-delayed modulation of firing in avian nucleus laminaris neurons. *J Neurosci* 16: 993–1007, 1996.
- Rothman JS, Young ED, Manis PB. Convergence of auditory nerve fibers onto bushy cells in the ventral cochlear nucleus: implications of a computational model. *J Neurophysiol* 70: 2562–2583, 1993.
- Segev I. Sound grounds for computing dendrites. *Nature* 393: 207–208, 1998.
- Simon J, Carr CE, Shamma S. A dendritic model of coincidence detection in the avian brainstem. *Neurocomputing* 26/27: 263–269, 1999.
- Smith DJ, Rubel EW. Organization and development of brain stem auditory nuclei of the chicken: dendritic gradients in nucleus laminaris. *J Comp Neurol* 186: 213–239, 1979.
- Smith PH. Structural and functional differences distinguish principal from nonprincipal cells in the guinea pig MSO slice. *J Neurophysiol* 73: 1653–1667, 1995.
- Smith ZD. Organization and development of brain stem auditory nuclei of the chicken: dendritic development in n. laminaris. *J Comp Neurol* 203: 309–333, 1981.
- Stotler W. An experimental study of the cells and connections of the superior olivary complex of the cat. *J Comp Neurol* 98: 401–432, 1953.
- Svirskis G, Dodla R, Rinzel J. Subthreshold outward currents enhance temporal integration in auditory neurons. *Biol Cybern* 89: 333–340, 2003.
- Svirskis G, Kotak V, Sanes D, Rinzel J. Sodium along with low-threshold potassium currents enhance coincidence detection of subthreshold noisy signals in MSO neurons. *J Neurophysiol* 91: 2465–2473, 2004.
- Traub RD, Wong RK, Miles R, Michelson H. A model of a CA3 hippocampal pyramidal neuron incorporating voltage-clamp data on intrinsic conductances. *J Neurophysiol* 66: 635–650, 1991.
- Warchol ME, Dallos P. Neural coding in the chick cochlear nucleus. *J Comp Physiol A Sens Neural Behav Physiol* 166: 721–734, 1990.
- Williams SR, Stuart GJ. Dependence of EPSP efficacy on synapse location in neocortical pyramidal neurons. *Science* 295: 1907–1910, 2002.
- Xu NL, Ye CQ, Poo MM, Zhang XH. Coincidence detection of synaptic inputs is facilitated at the distal dendrites after long-term potentiation induction. *J Neurosci* 26: 3002–3009, 2006.
- Yang L, Monsivais P, Rubel EW. The superior olivary nucleus and its influence on nucleus laminaris: a source of inhibitory feedback for coincidence detection in the avian auditory brainstem. *J Neurosci* 19: 2313–2325, 1999.
- Zhou Y, Carney LH, Colburn HS. A model for interaural time difference sensitivity in the medial superior olive: interaction of excitatory and inhibitory synaptic inputs, channel dynamics, and cellular morphology. *J Neurosci* 25: 3046–3058, 2005.